An Integrated Approach for Characterizing the Dynamic Behavior of the Wheel–Rail Interaction at Crossings

Zilong Wei, Anthonie Boogaard, Alfredo Núñez, *Senior Member, IEEE*, Zili Li, and Rolf Dollevoet

***Abstract*— This paper describes an approach for characterizing the dynamic behavior of the vehicle/track interaction at railway crossings. In the approach, we integrate in situ axle box acceleration (ABA) measurements with roving-accelerometer hammer tests to evaluate the influence of train speed, train moving direction (facing and trailing directions), sensor position (leading and rear wheels of a bogie), and the natural response of track structure on ABA signals. The analysis of data from multiple sensors contributes to the following findings: the major frequency bands of the vertical ABA are related to the natural frequencies of the crossing; thus, these ABA frequency bands are not greatly affected by variations in train speed, moving direction, and sensor position. The vibration energy concentrated at the major ABA frequency bands increases at higher train speeds, along the facing moving direction and from the leading wheel. The crossing rails vibrate as a combination of bending and torsion rather than solely bending at the major ABA frequency bands, since the vibrations of the wing rails are not synchronized. These results help enhance our understanding of the vehicle/track interaction at crossings and can be used to improve the dynamic response-based system for monitoring the condition of crossings.**

***Index Terms*— Axle box acceleration (ABA) measurement, railway crossing, roving-accelerometer hammer test, track dynamics, vehicle dynamics.**

I. Introduction

RAILWAY systems are a major mode of passenger and freight transportation worldwide. In the recent years, the increased demands on railway systems, including higher speed, greater capacity, and longer service time, have accelerated the deterioration of track infrastructure. In particular, crossings deteriorate more quickly than plain tracks because of the impact of the wheels on the rails [1] at geometric discontinuities (e.g., the gap between the closure rail and the crossing nose in Fig. 1). It is important to efficiently monitor the condition of crossings so that maintenance measures such as grinding and welding [2] can be used in a timely fashion on deteriorated crossings.

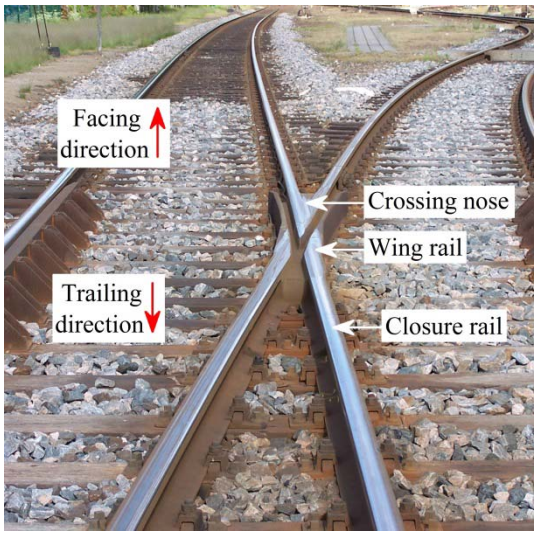

Fig. 1. Schematic of a crossing.

In the Dutch railway network, crossings are inspected by human visual inspection and ultrasonic measurement. Visual inspection involves visiting the tracks or watching videos of tracks, which requires a substantial number of man hours for large-scale railway networks. Ultrasonic measurement is better able to detect internal cracks but is not suitable for rail surface defects [3]. To fill the gap between the increased demands on the railway network and the low efficiency of the current inspection methodologies, a prompt diagnostic system is required.

Train-borne inspection systems based on axle box acceleration (ABA) measurement represent an automatic and efficient method for condition monitoring of track infrastructure [4]. The ABA system has been used to assess both periodic defects (e.g., corrugations [5] and wheel flats [6]) and isolated defects (e.g., squats [7], worn welds, and insulated joints [8]) on plain tracks. The detection mechanism employed by the ABA system relies on identifying changes in the characteristic response with respect to the nominal condition. At crossings, the application of the ABA system is more complicated because the measured ABA signals reflect responses related

Manuscript received November 16, 2017; revised February 26, 2018; accepted February 27, 2018. Date of publication April 3, 2018; date of current version September 17, 2018. This work was supported by the Dutch Technology Foundation STW under Grant 12246. The work of Z. Wei was supported by the China Scholarship Council under Grant 201206260104. The Associate Editor coordinating the review process was Dr. Anirban Mukherjee. *(Corresponding author: Zili Li.)*

The authors are with the Section of Railway Engineering, Faculty of Civil Engineering and Geosciences, Delft University of Technology, Delft 2628, The Netherlands (e-mail: z.wei@tudelft.nl; m.a.boogaard@tudelft.nl; a.a.nunezvicencio@tudelft.nl; z.li@tudelft.nl; r.p.b.j.dollevoet@tudelft.nl).

Color versions of one or more of the figures in this paper are available online at http://ieeexplore.ieee.org.

Digital Object Identifier 10.1109/TIM.2018.2816800

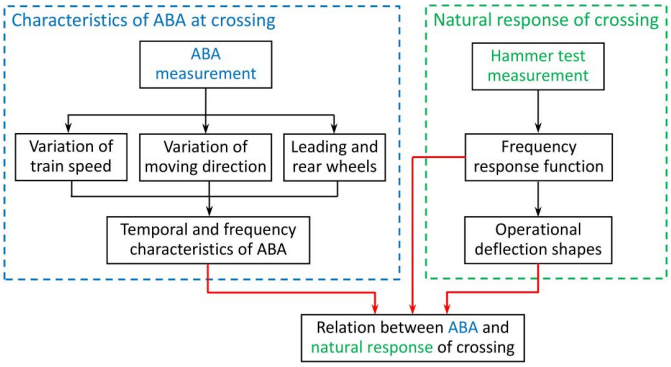

Fig. 2. Flowchart depicting the methodology in this paper.

to both inherent geometric discontinuities and undesirable defects.

It was recently demonstrated that the ABA system could identify certain types of crossing defects by properly correlating data from multiple sensors (ABA and 3-D profile measurements) over time [9]. This feasibility study was conducted under controlled constant test conditions (e.g., fixed train speed and moving direction), which rarely happen for the real life implementation using in-service trains. Therefore, the influence of various test conditions on the ABA signals must be studied to employ the system for condition monitoring purpose. Previous studies have shown that the characteristic frequencies of ABA on plain tracks are related to the natural behavior of the track structure [10]. If this is also the case at crossings, the natural response of crossings and their relationship with ABA must be investigated because the natural response can differ greatly between crossing types.

In this paper, we analyze the characteristics of ABA at crossings under various test conditions. These conditions include train speed, train moving direction (facing and trailing direction with respect to the crossing), sensor position (leading and rear wheels in a bogie), and crossing natural response. Several previous studies have examined ABA signals at crossings [11], [12], but they neither investigated the characteristics of ABA under various test conditions and nor combined ABA measurements with other methodologies (e.g., hammer tests [13]) to study the vehicle and track dynamics. We aim to fill this knowledge gap by correlating the ABA measurements with a roving-accelerometer hammer test. We expect that the results will not only enhance our understanding of the dynamic vehicle/track interaction but also advance the utility of the ABA system for condition monitoring of crossings. Fig. 2 illustrates the methodology of this paper.

II. In Situ ABA and Hammer Test Measurements

This paper uses *in situ* ABA and hammer test measurements. The measurements were conducted on a nominal crossing of the 54E1-1:9 type (with the UIC54 rail profile and a crossing angle of 1:9). The train operational speed over the crossing is limited to 40 km/h.

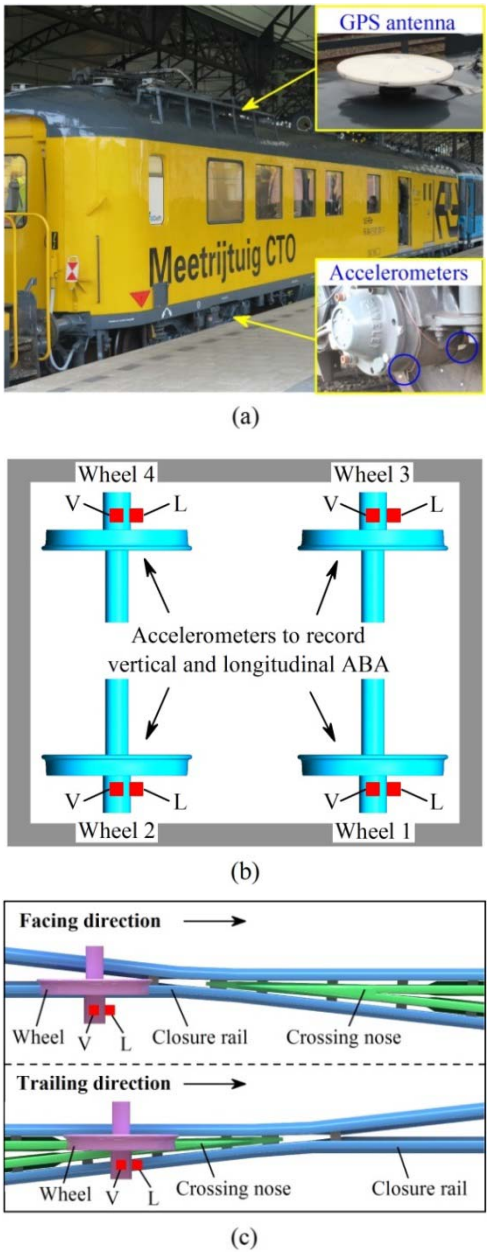

Fig. 3. (a) ABA measurement system with close-up views of the accelerometers and the GPS antenna. (b) Arrangement of accelerometers on a bogie. Letters V and L denote accelerometers mounted in the vertical and the longitudinal directions. (c) Moving direction of measurement coach. The wheel moves from the closure rail to the crossing nose in the facing direction and vice versa in the trailing direction.

A. ABA Measurement System

The ABA system includes three main components: accelerometers, a GPS antenna, and a tachometer, [see Fig. 3(a)]. Accelerometers were mounted on the axle boxes of a bogie to record the ABA signals [Fig. 3(b)], and the sampling frequency was set to 25.6 kHz. An ABA signal up to 3 kHz can be accurately captured over a wide range of speeds. A GPS antenna was installed on the train roof to record the position of the train. In addition, a tachometer was used to determine the train speed.

Table I lists the test scenarios for the ABA measurements. The ABA signals were acquired: 1) at two speeds,

TABLE I
TEST SCENARIOS FOR THE ABA MEASUREMENT

Item	Parameters
Train speed	28 km/h 36 km/h
Moving direction	Facing (from closure rail to crossing nose) Trailing (from crossing nose to closure rail)
Sensor position	Wheel 1 (leading wheel in facing direction) Wheel 2 (rear wheel in facing direction)

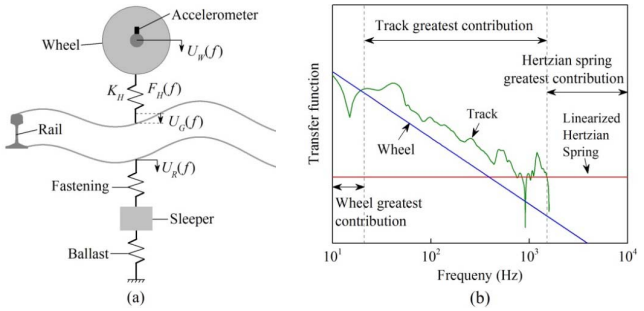

Fig. 4. (a) Schematic of the ABA measurement. (b) Components of the measured ABA.

28 and 36 km/h; 2) along two moving directions, facing and trailing; and 3) from two wheels, 1 and 2. The ABA measurement was conducted with a measurement coach [see Fig. 3(a)], which interferes with the regular train operation, and thus limits the availability of the measurement. In total, only six tests could be conducted and each scenario includes three repeated tests, leaving the opportunity for specifying only two train speeds. The speeds of 28 and 36 km/h were specified because: 1) they must not exceed the limit of 40 km/h; 2) they should significantly differ from each other to easily identify their influence on the ABA; and 3) they should be high enough to make the characteristics of ABA clearly observable, as higher train speed generally comes with greater energy concentration [10].

Fig. 4(a) shows a simplified model of the ABA measurement [14]. In the model, a wheel is simplified as a mass and interacts with the rail by means of a Hertzian spring. The ABA can be expressed as [14]

$$\ddot{U}_W(f) = -\frac{U_G(f)}{M_W[H_W(f) - H_R(f) - 1/K_H]} \tag{1}$$

where M_W is the wheel mass, K_H is the linearized stiffness of the Hertzian spring, $U_G(f)$ is the rail irregularity, and $U_R(f)$ is the rail displacement due to the dynamic component of the wheel–rail contact force $F_H(f)$. $H_W(f)$ and $H_R(f)$ are the transfer functions between the wheel–rail displacement and the force $F_H(f)$.

Equation (1) indicates that the measured ABA contains information for three components: the wheel, the track, and their interaction [see Fig. 4(b)]. In practice, the measured ABA signals may be affected by several interferences and noise, which may come from: 1) randomness in the vehicle/track interaction arising from wheelset hunting oscillations; 2) interference from degraded vehicle/track components, e.g., wheel flats; and 3) improper type selection and instrumentation of accelerometers.

The ABA signals were measured in the time domain. However, it is not straightforward to extract the characteristic dynamic response only by analyzing the waveform and the amplitude of the ABA signals. Frequency analysis is required because it can provide crucial information that is challenging to identify in the time domain. In general, the majority of the conventional time–frequency analysis techniques can be classified into two categories: linear transform (e.g., short-time Fourier transform (STFT) [15] and wavelet transform (WT) [16]) and quadratic transform (e.g., Wigner–Ville distribution (WVD) [17] and its variants). The STFT uses a fixed window size such that a tradeoff must be made between time and frequency resolutions. The WT employs scaling and translating windows that can effectively preserve the transient characteristics of a signal. However, the WT is a nonadaptive method and the time–frequency presentation relies on a predetermined basis, independent of the analyzed signal. The WVD can provide a high resolution of the time–frequency representation, but it is subjected to the interference of cross-term. More sophisticated quadratic time–frequency analysis methods have recently been developed to overcome this drawback, such as the combination of the adaptive kernel with the Bayesian compressive sensing techniques [18]–[21].

In Fig. 5, we compare the performance of four time–frequency analysis methods, including the continuous WT (CWT, nonadaptive linear method), synchrosqueezing transform [22] (SST, nonadaptive linear method), WVD (nonadaptive quadratic method), and empirical mode decomposition [23] (EMD, adaptive method). The ABA signals to be processed are measured with a sampling frequency of 25.6 kHz, and the frequency of interest is 150–800 Hz. In general, the WVD has the poorest performance due to the cross-term interference. Note that the new methods as proposed in [18]–[21] could tackle this drawback. The CWT, SST, and EMD can extract the major characteristic frequencies from the ABA. In this paper, the CWT is used because: 1) the sampling frequency of the ABA is 25.6 kHz and the interested frequency is 150–800 Hz, such that the limitation of the CWT (low time resolution at very low-frequency range and low-frequency resolution at very high frequency) can be significantly reduced; 2) the capability of the CWT in processing ABA signals has been demonstrated in the literature [7], [24], [25]; and 3) the ABA signals are not very noisy due to the thorough type selection and the instrumentation of accelerometers, and it is not difficult to distinguish the characteristic frequencies.

To achieve a satisfactory time–frequency representation in various complicated scenarios, many advanced techniques with adaptive and automated features have been developed, such as decomposition [26], [27], extraction [28]–[30] and enhancement [31], [32] of noisy, multivariate, multicomponent, nonlinear, and nonstationary signals as well as feature detection (e.g., motor fault detection [33], disease diagnosis [34], and contact wire irregularities [35]).

In the CWT, the convolutions of the analyzed signal are calculated with a group of scaled and shifted wavelet functions.

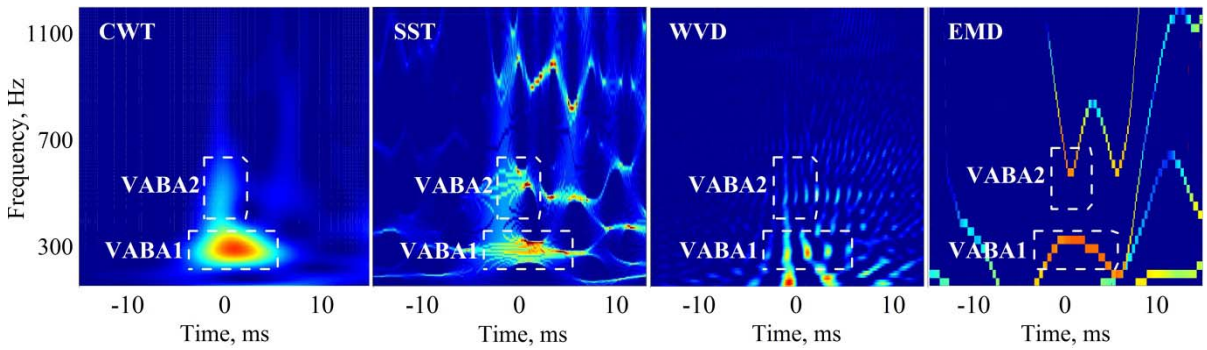

Fig. 5. Time–frequency representation of the ABA with CWT, SST, WVD, and EMD. VABA1 and VABA2 indicate the major ABA frequency bands at 265–305 and 510–600 Hz.

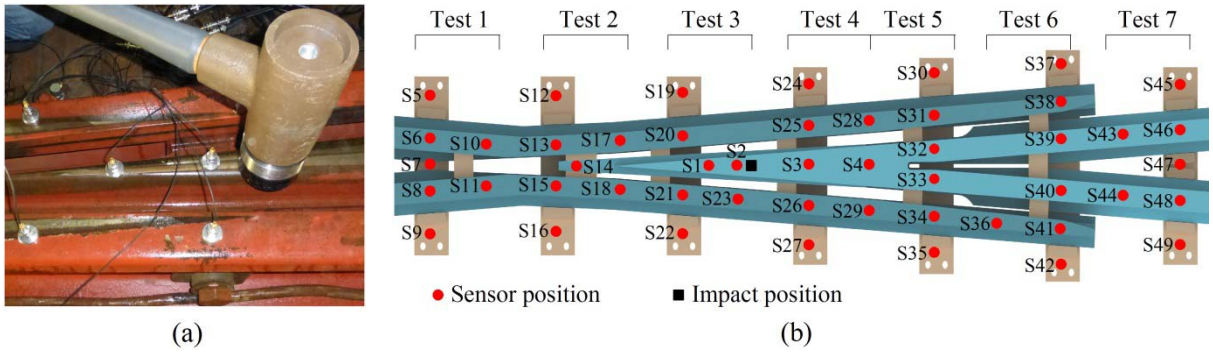

Fig. 6. *In situ* hammer test. (a) Hammer and accelerometers. (b) Arrangement of accelerometers.

The wavelet coefficients $W_n(s)$ of the analyzed signal x can be represented as [16]

$$W_n(s) = \sum_{n'=0}^{N-1} x_{n'} \psi^* \left[\frac{(n'-n)\delta_t}{s} \right] \tag{2}$$

where ψ is the mother wavelet, s is the wavelet scale, N is the number of points in the time series, $n' = 0, \ldots, N-1$, δ_t is the time step, n is the continuous variable for translation, s is the wavelet scale, $*$ presents a complex conjugate, and $\psi^*[((n'-n)\delta_t/s)]$ is the family of wavelets deduced from the mother wavelet by different translation and scaling methodologies. Here, the Morlet function was used as the mother wavelet. Thereafter, the wavelet power spectrum (WPS) was calculated through the square of the wavelet coefficients $|W_n^2(s)|$. To quantify the distributions of the WPS at each frequency, the global WPS (GWPS) $\bar{W}^2(s)$ was calculated and expressed as

$$\bar{W}^2(s) = \frac{1}{N} \sum_{n=0}^{N-1} |W_n^2(s)|. \tag{3}$$

B. Setup of the Hammer Test Measurement

Impact measurements are commonly used to characterize the dynamics of the track structure [36] and derive the parameters of the track components [37]. In the literature, several impact methodologies are specified. For example, the track vibrations in the low-frequency range (below 150 Hz) mainly correspond to the track substructure components (e.g., subgrade and ballast) [38]; thus, the falling weight test [39] is best able to provide sufficient energy to fully excite these components. In contrast, the track vibrations at 150–800 Hz are closely related to the rails and track superstructure components (e.g., fastening, railpad, and sleeper); these vibrations are best tested using a sledgehammer with a soft tip. At higher frequencies (800–3000 Hz), the structural vibrations are dominated by the rails, and thus a light hammer with a hard tip should be used.

In this paper, an instrumented sledgehammer (PCB-086D50) with a plastic tip was used [see Fig. 6(a)]. To record the vertical vibrations of the crossing, seven accelerometers (Brüel & Kjær 4514-004) were placed on the railhead and baseplate using a magnet base. The hammer and accelerometers were connected to a data logger (MBBM-PAK-MKII). The sampling frequency of the force and acceleration signals was set to 4096 Hz, and the duration of the signals was set to 1000 ms.

In the literature, the natural behavior of railway tracks is often measured at fixed positions [13], [40], [41]; two typical positions are the on support and the midspan [42], [43]. This simplified setup is appropriate for plain tracks, but is less useful at crossings due to their complex structure and discontinuous geometry. This implies that the measured vibrations may differ significantly at each sensor position, leaving the dynamic behavior of the entire structure unclear. Therefore, it is preferable to highlight the global nature of the crossing by measuring the vibrations at many positions. The hammer test employs a roving-accelerometer approach [44]–[46].

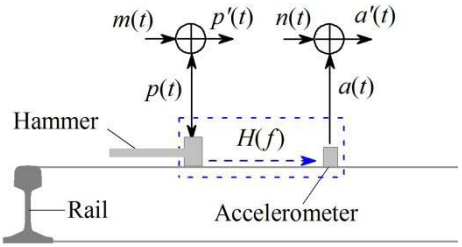

Fig. 7. Schematic of the hammer test.

The impact occurred in the same position throughout measurements, while the accelerometers were rearranged seven times. Fig. 6(b) shows the arrangement of the accelerometers. Using the roving-accelerometer approach, the crossing vibrations at 49 positions were recorded, covering the length of six sleeper spans (approximately 3.7 m).

Fig. 7 shows the model of the hammer test. In Fig. 7, $p(t)$ indicates the force signal, $a(t)$ indicates the response signal, while $m(t)$ and $n(t)$ indicate the interferences.

The frequency response function (FRF) can be calculated using the cross input–output spectrum and the input autospectrum [47]

$$H_1(f) = \frac{S_{p'a'}(f)}{S_{p'p'}(f)}. \tag{4}$$

In addition, the FRF can also be calculated by using the output autospectrum and the cross input–output spectrum

$$H_2(f) = \frac{S_{a'a'}(f)}{S_{a'p'}(f)} \tag{5}$$

where $S_{p'a'}(f)$ is the cross-spectrum between force and acceleration, $S_{p'p'}(f)$ is the autospectrum of the force, and $S_{a'a'}(f)$ is the autospectrum of acceleration.

Under ideal test conditions, (4) and (5) should provide the same results. However, the calculated FRF may be affected by several interferences, the majority of which may come from the following.

1) Improper type selection and instrumentation of the hammer and the accelerometers. For example, the response curve of the hammer does not fit the frequency of interest.
2) Random human factors, such as nonidentical impact position and direction among tests.
3) The measured response $a'(t)$ is interfered by external inputs other than $p(t)$, such as the passing of vehicles nearby the test site.
4) The nonlinear relation between the input $p(t)$ and the response $a(t)$, such as the nonlinear behavior of the fastening and ballast.

The influence of the aforementioned interferences can be indicated by the coherence function $\gamma^2(f)$, expressed as

$$\gamma^2(f) = \frac{H_1(f)}{H_2(f)} = \frac{|S_{a'p'}(f)|^2}{S_{a'a'}(f)S_{p'p'}(f)}. \tag{6}$$

In practice, the coherence γ^2 is always greater than 0 while less than 1. In the *in situ* hammer test, the analysis can be regarded as high quality, if the value γ^2 exceeds 0.9.

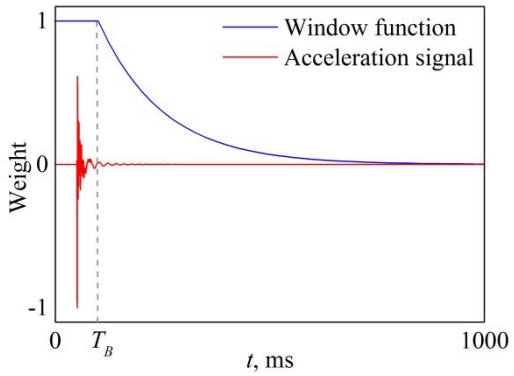

Fig. 8. Block exponential window function.

To reduce the leakage of the transient-type signals, a block exponential window [48] is applied. The exponential window can reduce the response at the end of the time period, while leaving the response at the beginning unaltered. However, the exponential window adds damping in the measured system, and a pretrigger is commonly used to fully capture the response. Thus, the exponential window is required only for the last part of the response. By combining with a block window, the response is not altered by changing the length of the pretrigger and the added damping can be kept to a minimum. Fig. 8 shows the window function, which is expressed as

$$w(t) = \begin{cases} 1 & \text{if } t \le T_B \\ e^{-(t-T_B)/\tau} & \text{if } t > T_B \end{cases} \tag{7}$$

where T_B is the length of the block and τ is the decay rate. Here, the values of T_B and τ were set to 100 and 150 ms, respectively.

III. Characteristic Behavior of Wheel–Rail Interaction at a Crossing

The ABA measurements were performed at a crossing with various train speeds, moving directions, and sensor positions to determine their influence on the characteristics of the ABA.

A. Train Speed and Moving Direction

In this section, we analyze the influence of train speed and moving direction on the ABA signals. During the measurements, the train ran over the crossing at both train speeds (28 and 36 km/h) and moving directions (facing and trailing directions, see Fig. 3). The ABA signals were recorded from the rear wheel (Wheel 2 in the facing direction and Wheel 1 in the trailing direction) to avoid disturbance from nonidentical test conditions.

Fig. 9(a)–(d) shows the vertical ABA (VABA) acquired from the rear wheel. In Fig. 9, the origin of the abscissa aligns with the crest of the peaks A and F. In general, the variation in train speed does not greatly affect the waveforms of the VABA. With the increase of train speed, the amplitudes of the VABA increase by 30%–77% at arrows A–C in the facing direction [Fig. 9(a) and (b)] and by 13%–38% at arrows D–F in the trailing direction [Fig. 9(c) and (d)]).

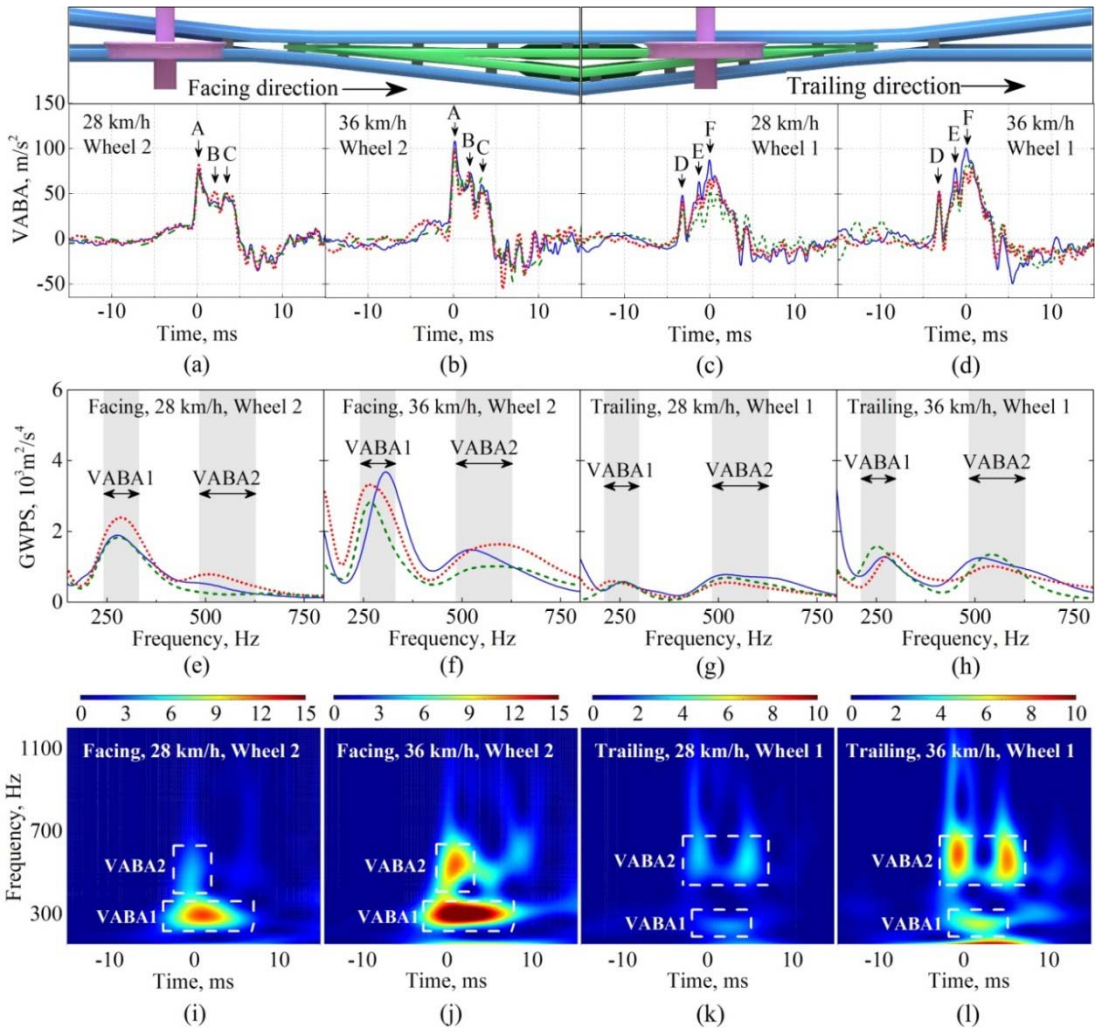

Fig. 9. VABA acquired from the rear wheel. (a)–(d) Time history. The solid line (——), dashed line (- - -), and dotted line (···) indicate three independent tests. (e)–(h) GWPS of VABA. Letters VABA1 and VABA2 indicate the major frequency bands at 265–305 and 510–600 Hz in the facing direction, while at 240–290 and 505–545 Hz in the trailing direction. (i)–(l) WPS of VABA.

Fig. 9(e)–(h) shows the GWPS of the VABA while Fig. 9(i)–(l) shows the WPS of the VABA. The GWPS was calculated from the ABA signals between −28 and 28 ms (equal to the rolling distance of 436 mm at 28 km/h and 560 mm at 36 km/h) to reduce the disturbance from vibrations far away from the wheel–rail impact. The frequencies of interest were between 150–800 Hz, because: 1) the low-frequency components below 150 Hz are mainly relevant to the track substructure components (e.g., subgrade and ballast) rather than the crossing rails; and 2) the high-frequency components above 800 Hz have much lower energy than the lower frequency components, making them less visible at the same scale.

At both the speeds, the major frequency bands of VABA occurred at 265–305 and 510–600 Hz in the facing direction; they shifted slightly to 240–290 and 505–545 Hz in the trailing direction. This information indicates that these major frequency bands are not greatly affected by variations in train speed and moving directions. With the increase in train speed, the GWPS acquired in the facing direction [Fig. 9(e) and (f)] increases by approximately 54%–60% for the first major frequency band and by approximately 93%–107% for the second major frequency band. Meanwhile, at the first major frequency band, the GWPS in the facing direction [Fig. 9(e) and (f)] increases by 129%–227% compared to the value in the trailing direction [Fig. 9(g) and (h)]. Between the two directions, the slight shift in the major frequency bands can be attributed to different wheel–rail impact positions. That is, the wheel impacts the crossing nose in the facing direction but the wing rail in the trailing direction, thus affecting the dynamic response of the system.

As shown in Fig. 9, the measured ABA signals demonstrate good repeatability among the three repeated tests of all the scenarios with respect to: 1) the waveforms and the amplitudes in the time domain; and 2) the major frequencies and energy concentration in the frequency domain. Minor deviations among tests can be attributed to the aforementioned interferences, such as wheelset hunting oscillations.

Based on the analysis in Section III-A, we suggest that the train speed and moving direction affect the characteristics of

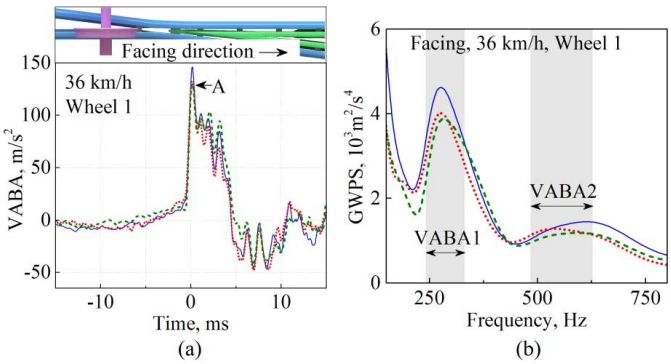

Fig. 10. VABA from the leading wheel. The signals were acquired at 36 km/h in the facing direction. (a) Time history. The solid line (—), dashed line (---), and dotted line (···) indicate three independent tests. (b) GWPS of the VABA. Letters VABA1 and VABA2 indicate the major frequency bands at 275–285 and 530–620 Hz.

the VABA in the following ways.

1) The moving direction does not significantly affect the major frequency bands of the VABA.
2) In both facing and trailing directions, variations in train speed do not strongly influence the major frequency bands of the VABA.
3) The energy concentrated at the major frequency bands of the VABA depends on the moving direction.
4) The amplitude of the VABA and vibration energy concentrated at the major frequency bands increase with the train speed.

B. Sensor Position

In this section, we compare the VABA acquired from Wheels 1 and 2. The difference between the two wheels is that Wheel 1 is the leading wheel in the facing direction, running over the crossing ahead of Wheel 2; in contrast, Wheel 2 becomes the leading wheel in the trailing direction.

Fig. 10 shows the VABA acquired from Wheel 1 at 36 km/h in the facing direction. The two major frequency bands of the VABA occur at 275–285 and 530–620 Hz [Fig. 10(b)]. These frequency bands are generally consistent with those from Wheel 2 [265–305 and 520–590 Hz, see Fig. 9(f)]. However, the leading wheel (Wheel 1) generally has a larger amplitude and higher vibration energy. For example, at arrow A, the amplitude of the VABA for Wheel 1 [130–146 m/s^2 in Fig. 10(a)] is 30%–35% larger than that for Wheel 2 [100–108 m/s^2 in Fig. 9(b)]. As another example, at the first major frequency band, the GWPS from Wheel 1 increases by 21%–32% compared with Wheel 2. Deviations in the amplitude, vibration energy, and major frequency bands of the VABA between the two wheels can be explained by randomness associated with the wheel–rail interactions, as well as the different loading conditions. When the rear wheel (Wheel 2) impacts the crossing nose, the latter is preloaded by the leading wheel (Wheel 1), changing the mass participating in the structural vibrations and the stiffness of the system (e.g., worn fastening [49] and ballast [50]).

Based on the analysis in Section III-B, we suggest that the sensor position has the following effects on the characteristic VABA.

1) The different sensor positions do not significantly affect the two major frequency bands of the VABA.
2) The leading wheel is associated with a larger VABA amplitude and greater vibration energy.

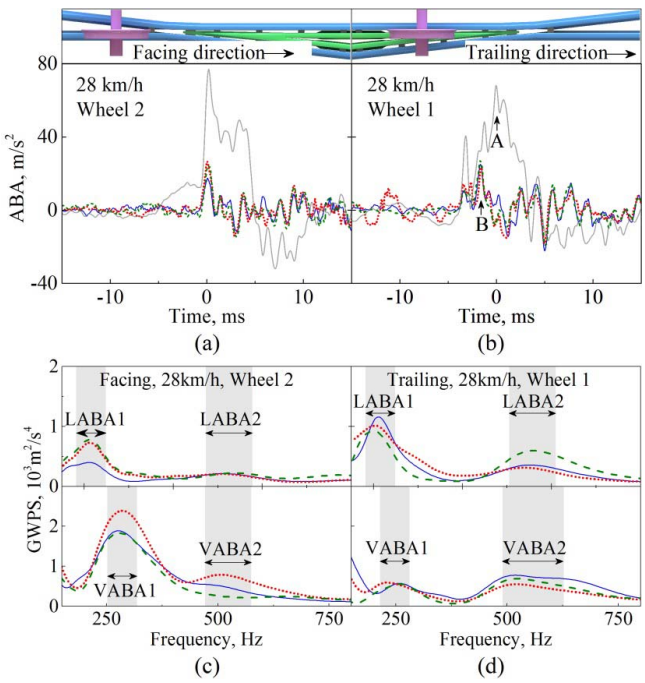

Fig. 11. Comparison between the LABA and the VABA. The signals were acquired from the rear wheel at 28 km/h. (a) and (b) Time history. The solid line (—), dashed line (---), and dotted line (···) indicate the LABA from three independent tests, while the shadow solid line (—) indicates the VABA. (c) and (d) GWPS of the ABA. Letters VABA1 and VABA2 indicate the major frequency bands of the VABA, while letters LABA1 and LABA2 indicate the major frequency bands of the LABA.

C. Relation Between Longitudinal and Vertical ABA

It is illustrated in [7] that the longitudinal ABA (LABA) is more sensitive to minor rail defects (e.g., light squats) than the VABA. Therefore, a better understanding of the characteristics of the LABA and its relationship to the VABA will help with condition monitoring of crossings. In this section, we analyze the characteristics of the LABA.

Fig. 11(a) and (b) compares the LABA and the VABA. The maximum amplitude of the LABA is 67%–76% smaller than the VABA in the facing direction and 58%–72% smaller in the trailing direction. In addition, the variations in the LABA and the VABA are not synchronized, as the maximum LABA [arrow B in Fig. 11(b)] occurs prior to the maximum VABA [arrow A in Fig. 11(b)]. This behavior can be attributed to the complex wheel–rail contact geometry and the evolution of the two-point contact (with one contact patch on the wing rail and the other on the crossing nose) [51], which will be analyzed in the further research.

Fig. 11(c) and (d) compares the GWPS of the LABA and the VABA. The major frequency bands of the LABA occur at 205–215 and 500–540 Hz in the facing direction and at 200–210 and 540–560 Hz in the trailing direction.

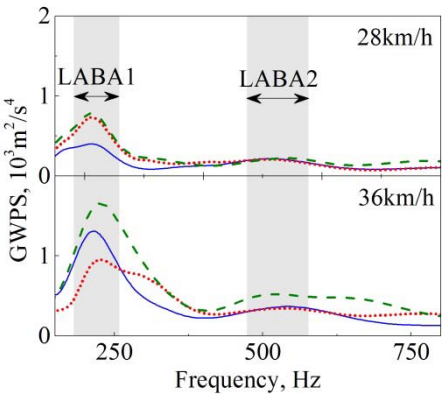

Fig. 12. GWPS of the LABA in the facing direction. The signals were acquired from the rear wheel. The solid line (——), dashed line (---), and dotted line (···) indicate three independent tests. Letters LABA1 and LABA2 indicate the major frequency bands.

Therefore, as with the VABA, the moving direction does not significantly affect the major frequency bands of the LABA.

Fig. 12 compares the GWPS of the LABA between 28 and 36 km/h. In Fig. 12, the variations in train speed do not strongly affect the major frequency bands of the LABA. Meanwhile, with the increase of train speed, the GWPS of the LABA increases by 111%–138% at the first major frequency band and by 65%–133% at the second major frequency band.

Based on the analysis in Section III-C, we conclude the following regarding the characteristics of the LABA.

1) The major frequency bands of the LABA are not strongly affected by the moving direction.
2) Variations in train speed significantly affect the vibration energy at the major frequency bands of the LABA rather than the major frequency bands themselves, similar to the VABA.

IV. Relationship Between the Characteristics of the ABA and the Natural Response of a Crossing

Previous studies have shown that the characteristic frequencies of the VABA correspond to the natural frequencies of plain track structures [10]. Therefore, it is important to understand the natural response of crossings to calibrate and improve the ABA system.

The natural response of the crossing was determined based on the roving-accelerometer hammer tests [see Fig. 6(b)]. Fig. 13 shows examples of the impact force and acceleration signals for Tests 1–7. The starting point of the hammer impact was aligned to 50 ms, as denoted by the dashed line (---). In all tests, the impact force had a duration of approximately 2 ms and an amplitude of approximately 25 kN. Since it takes time for vibration energy to propagate from the impact position to the sensor position, the response of the crossing rail was delayed with respect to the dashed line. The delay time varied among the accelerometers depending on the distance between the impact position and the sensor position. For example, the delay time for Tests 1 and 7 was much longer than that for Tests 3 and 4.

The accelerance function was calculated using (4). Fig. 14(a) shows the accelerance function. To highlight the global nature of the structure, the accelerance calculated from accelerometers S1–S4 [Fig. 6(b)] was averaged. Fig. 14(b) shows the coherence function from accelerometers S1–S4. At the frequency of interest (150–800 Hz), the coherence is above 0.97. This demonstrates the reliability of the hammer test, i.e., the aforementioned interferences and noise have little effect on the hammer test.

In Fig. 14(a), four natural frequencies of the crossing, namely, 265, 490, 548, and 621 Hz, are dominant at 150–800 Hz. Comparing Figs. 8–10 with Fig. 14(a), it is observed that the crossing natural frequency of 265 Hz is near the first major VABA frequency band of 240–305 Hz. In addition, the crossing natural frequencies at 490, 548, and 621 Hz are near the second major VABA frequency band of 510–620 Hz. The frequency components are not exactly the same, probably due to the different loading conditions. The crossing was preloaded by vehicles during the ABA measurements, but this preloading was absent in the hammer tests. The wheel and the hammer may not have impacted at precisely the same position, which could also affect the FRF.

To gain insight into the dynamics of the crossing, the operational deflection shapes (ODSs) were analyzed. The ODSs are the spatial representation of the FRF at each frequency [52]. Comparing ODSs with mode shapes, the former can be measured directly and do not depend on postprocessing parameters, e.g., curve fitting for extracting mode shapes.

Fig. 15 shows the ODSs of crossing rails (including the closure rail, the wing rail, and the crossing nose) at two phases: the phase with the maximum impact force [Fig. 15(a)] and when the force reaches zero [Fig. 15(b)]. Fig. 15 demonstrates that lower natural frequencies generally correspond to longer ODS wavelengths. At all the natural frequencies examined, the vibrations of the crossing rails are not solely derived from bending because the vibrations of two wing rails were not synchronized, as shown by arrows W1 and W2. Instead, the vibrations are a combination of bending and torsion, which is common for asymmetric structures.

Fig. 16 shows the ODSs of the crossing nose at 60 phases of a full vibration cycle to analyze the evolution of the shape and the amplitude. At the natural frequency of 265 Hz, the ODS amplitude is smaller than the amplitudes at higher natural frequencies. This phenomenon may be related to the different effective mass participating in the structural vibration. That is, the mass of the system commonly participates less in structural vibrations at higher frequencies. After the crossing nose divides into two separate pieces, the two pieces vibrate with different amplitudes at 490 and 548 Hz, as indicated by arrows N1 and N2. This behavior suggests that the vibrations of the crossing nose also arise from a combination of bending and torsion.

In summary, the major frequency bands of the VABA (240–305 and 510–620 Hz) are related to the crossing natural frequencies (265, 490, 548, and 621 Hz). As a consequence, variations in train speed, train moving direction, and sensor position do not significantly affect the major frequency bands of the VABA. In addition, the vibrations of crossing rails

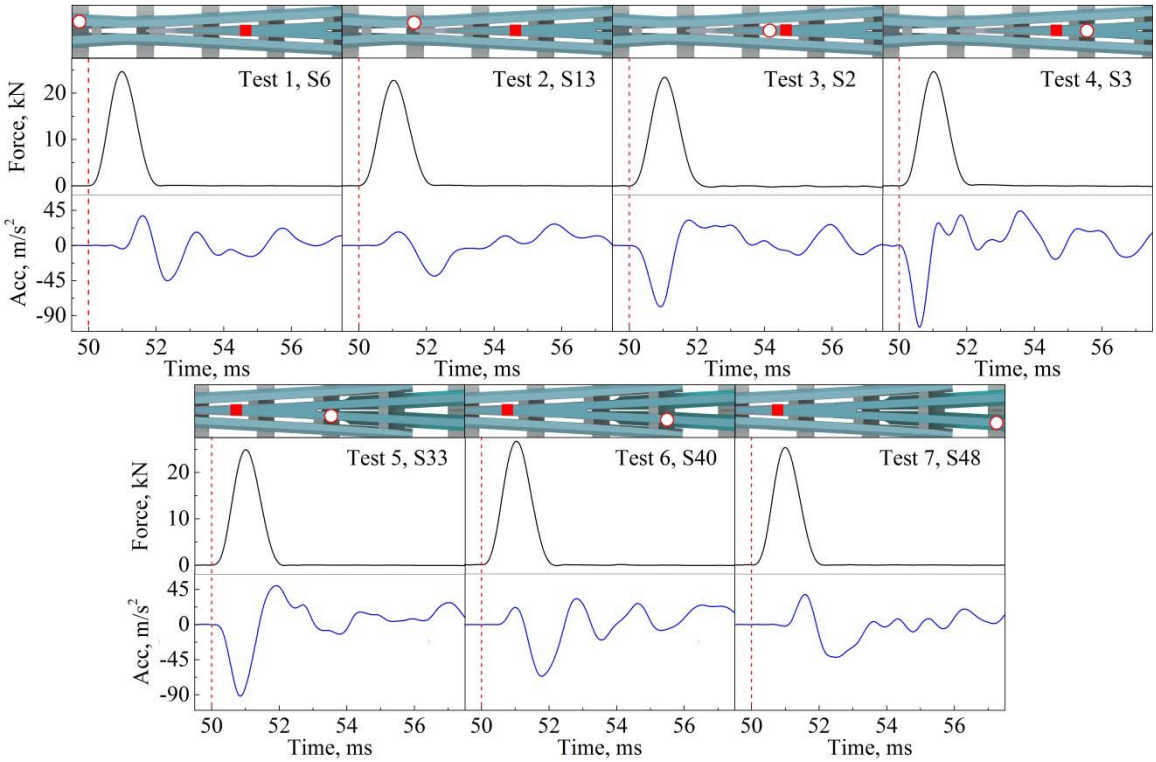

Fig. 13. Examples of the hammer impact force and acceleration signals. The symbols (■) and (◯) indicate the impact position and the sensor position. The dashed line (---) indicates the beginning of the hammer impact at 50 ms.

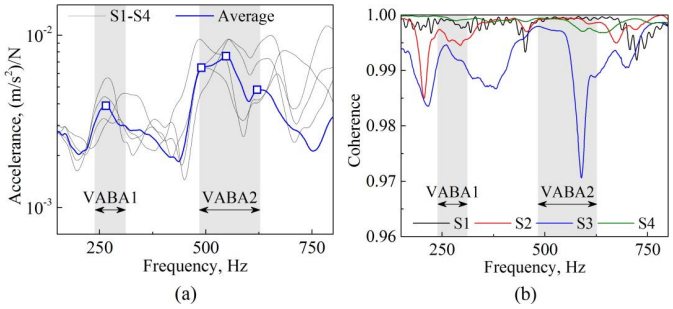

Fig. 14. FRF of crossing (a) accelerance and (b) coherence. The symbols (□) indicate the natural frequencies of the crossing at 265, 490, 548, and 621 Hz. Letters VABA1 and VABA2 indicate the major frequency bands at 240–305 and 510–620 Hz.

at these frequency bands are a combination of bending and torsion, because the vibrations of the two wing rails are not synchronized.

V. Discussion

A. Improving the ABA-Based Condition Monitoring System

Recently, the ABA system has demonstrated the capability of inspecting certain types of crossing degradation (e.g., squats [12] and uneven deformation on crossing rails [9]) by identifying the change in the dynamic response with respect to the nominal condition. In addition, preventative maintenance actions (e.g., grinding and welding) can be suggested based on the evaluation. However, the ABA measurements in the previous studies were performed at a controlled constant condition, i.e., at a fixed train speed, along a fixed moving direction and on a fixed crossing type, which limits their application for more generalized scenarios. In this paper, we analyzed the characteristics of the ABA under various test conditions. Because the ABA measurement was conducted on a nominal crossing, the obtained information can serve as the baseline. By comparing the baseline with the ABA measured at different time periods, we were able to identify the changes in the dynamic response to guide maintenance actions. In addition, the obtained information can also be integrated with the condition monitoring systems in the previous studies [9], [12] and improve their performance for generalized scenarios without the limitations on train speed, moving direction, and crossing type.

In this paper, the ABA measurement was conducted with a measurement coach [see Fig. 3(a)], which interferes with the regular train operation, and thus limits the availability of the measurement. In total, only six tests could be conducted. Alternatively, if in-service trains are instrumented with a similar ABA system, the crossing can be intensively measured without interfering the regular train operation. With more measured data, advanced methods such as trend analysis, probabilistic technique, machine learning, and artificial intelligence [53]–[56] can be applied to improve the reliability of the analysis and make better decisions for maintenance actions.

B. Uncertainty of Measurements

In both the ABA and hammer test measurements, the presence of random factors may induce uncertainties into the analysis. For example, the hammer may not impact the rail

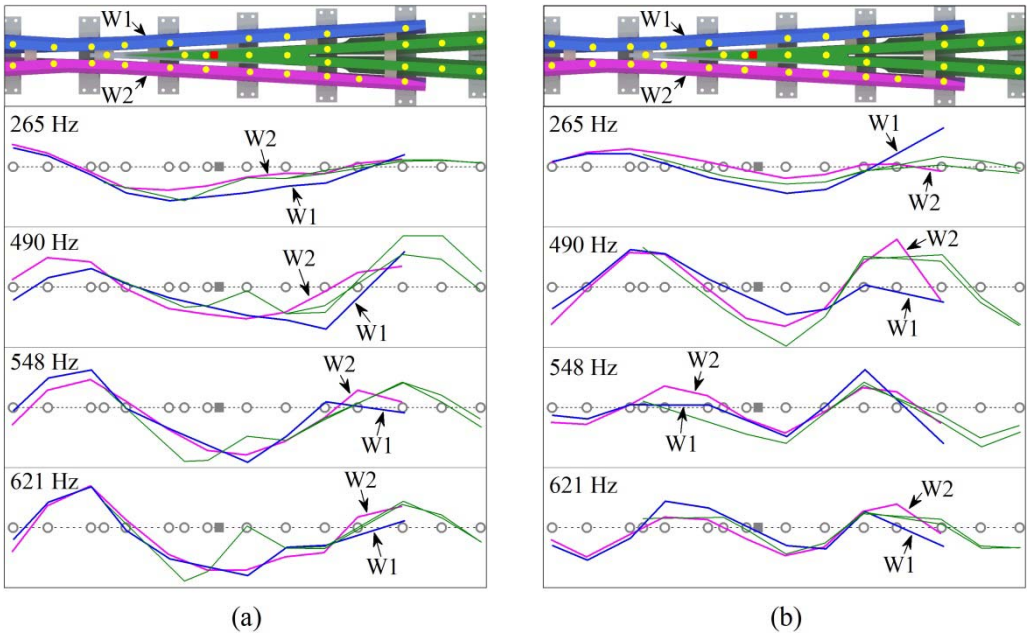

Fig. 15. ODSs of crossing rails at the crossing natural frequencies of 265, 490, 548, and 621 Hz. (a) Phase with the maximum impact force. (b) Phase where the impact force reached zero. The symbols (■) and (◯) indicate the impact position and the sensor position. Letters W1 and W2 indicate the nonsynchronized vibrations of the two wing rails.

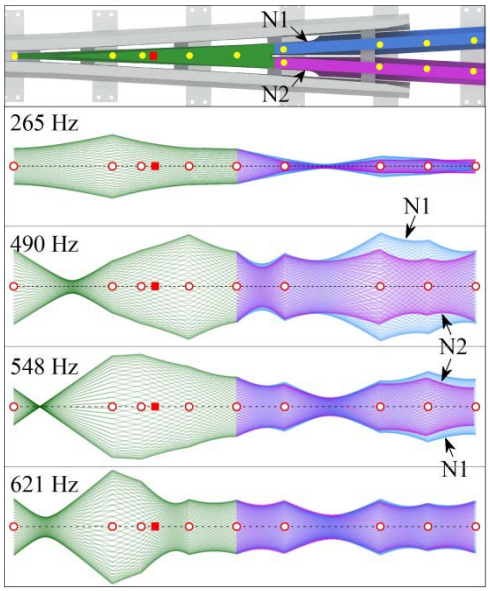

Fig. 16. ODSs of the crossing nose at 60 phases of a full vibration cycle. The ODSs are symmetric about the stationary state, i.e., the dashed line (---). The symbols (■) and (◯) indicate the impact position and the sensor position. Letters N1 and N2 indicate the nonidentical vibration amplitudes of the two pieces of the crossing nose.

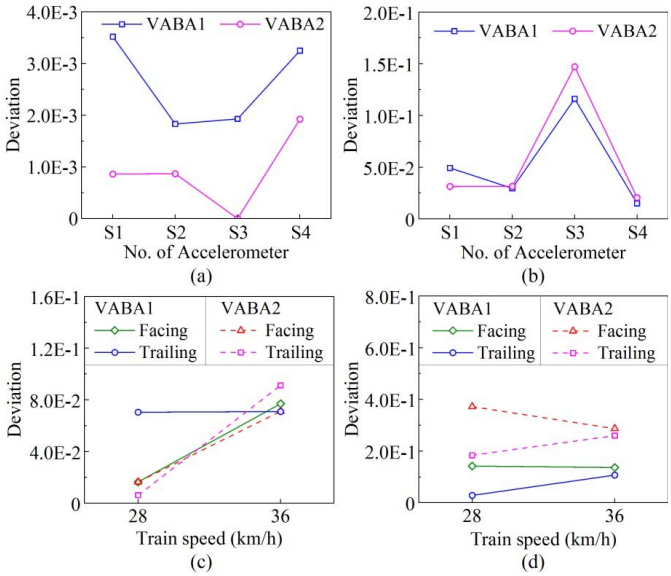

Fig. 17. Uncertainty of (a) and (b) hammer test and (c) and (d) ABA measurement evaluated by standard deviation among tests. (a) Crossing natural frequencies at VABA1 and VABA2. (b) Accelerance at crossing natural frequencies. (c) Major ABA frequencies VABA1 and VABA2. (d) GWPS at major ABA frequencies.

at exactly the same position and direction, and the wheelset may not run over the crossing along the exact same trajectory. In this paper, the uncertainty of measurements is evaluated by analyzing the standard deviation [57] of the measured signals among several independent tests. To facilitate the comparison between different items, the measured signals are normalized by dividing by their arithmetic mean.

Fig. 17 shows the standard deviation of the measured signals among tests. For the hammer test, the following uncertainties can be found: 1) the deviation of the crossing natural frequencies is much smaller than the accelerance at these frequencies; 2) the deviation of the crossing natural frequencies at VABA1 is larger than those at VABA2; and 3) at the accelerometer S3, the large deviation of accelerance is not accompanied by a large deviation of the crossing natural frequencies. Meanwhile, the following uncertainties can be found in the ABA measurement: 1) the deviation of the major ABA frequencies is significantly smaller than the

GWPS at these frequencies; 2) the deviation of the major ABA frequencies generally increases with train speed; and 3) in the trailing direction, the deviation of the GWPS is larger than that in the facing direction. Moreover, the ABA measurement has more significant uncertainties than the hammer test, which may be due to more significant randomness involved in the ABA measurement.

VI. Conclusion

In this paper, we characterized the dynamic behavior of the wheel–crossing interaction under various conditions. These conditions include the train speed, moving direction (facing and trailing directions with respect to the crossing), and sensor position (leading and rear wheels of a bogie). In addition, a roving-accelerometer hammer test was conducted to address the relationship between the major frequencies of the ABA and the crossing natural response. We draw the following conclusions from the results of this paper.

1) The correlation between the ABA and the hammer test measurements indicates that the major frequency bands of the VABA at 240–305 and 505–620 Hz are related to the natural frequencies of the crossing at 265, 490, 548, and 621 Hz. Therefore, the major frequency bands of the VABA are not greatly affected by variations in train speed, moving direction, or sensor position.
2) The amplitude of the VABA and the energy concentrated at the major frequency bands depend on train speed, moving direction, and sensor position. In particular, higher vibration energy occurs at faster train speeds, along the facing moving direction and from the leading wheel.
3) At the characteristic frequency bands of the VABA, the vibrations of the crossing rails are a combination of bending and torsion rather than pure bending, because the vibrations of the two wing rails are not synchronized.
4) Variations in train speed and moving direction do not significantly affect the major frequency bands of the LABA, which are similar to those of the VABA.

In the future work, the characteristic behavior of the wheel–rail interaction at a wider variety of crossings should be studied under more generalized test conditions (e.g., accounting for various traction, braking, and friction conditions). This analysis will require information from multiple sources, including ABA measurements, hammer tests, and other data such as profile measurements. This information can be used to develop a database for evaluating the condition of crossings and determining the amount of degradation present. Based on this information, threshold values for performing maintenance actions could also be developed to extend the service life of crossings.

Acknowledgment

The authors would like to thank the assistance from C. Shen and J. Hendriks during the *in situ* measurements.

References

[1] E. Kassa and J. C. O. Nielsen, "Dynamic train–turnout interaction in an extended frequency range using a detailed model of track dynamics," *J. Sound Vibrat.*, vol. 320, nos. 4–5, pp. 893–914, 2009.

[2] C. Wan, V. L. Markine, and I. Y. Shevtsov, "Improvement of vehicle–turnout interaction by optimising the shape of crossing nose," *Vehicle Syst. Dyn.*, vol. 52, no. 11, pp. 1517–1540, 2014.

[3] M. P. Papaelias, C. Roberts, and C. L. Davis, "A review on non-destructive evaluation of rails: State-of-the-art and future development," *Proc. Inst. Mech. Eng. F, J. Rail Rapid Transit*, vol. 222, no. 4, pp. 367–384, 2008.

[4] J. S. Lee, S. Choi, S.-S. Kim, C. Park, and Y. G. Kim, "A mixed filtering approach for track condition monitoring using accelerometers on the axle box and bogie," *IEEE Trans. Instrum. Meas.*, vol. 61, no. 3, pp. 749–758, Mar. 2012.

[5] M. Bocciolone, A. Caprioli, A. Cigada, and A. Collina, "A measurement system for quick rail inspection and effective track maintenance strategy," *Mech. Syst. Signal Process.*, vol. 21, no. 3, pp. 1242–1254, 2007.

[6] S. Alfi and S. Bruni, "Estimation of long wavelength track irregularities from on board measurement," in *Proc. 4th IET Int. Conf. Railway Condition Monitor.*, 2008, p. 16.

[7] M. Molodova, Z. Li, A. Núñez, and R. Dollevoet, "Automatic detection of squats in railway infrastructure," *IEEE Trans. Intell. Transp. Syst.*, vol. 15, no. 5, pp. 1980–1990, Oct. 2014.

[8] M. Molodova, M. Oregui, A. Núñez, Z. Li, and R. Dollevoet, "Health condition monitoring of insulated joints based on axle box acceleration measurements," *Eng. Struct.*, vol. 123, pp. 225–235, Sep. 2016.

[9] Z. Wei, A. Núñez, Z. Li, and R. Dollevoet, "Evaluating degradation at railway crossings using axle box acceleration measurements," *Sensors*, vol. 17, no. 10, p. 2236, 2017.

[10] M. Molodova, Z. Li, A. Núñez, and R. Dollevoet, "Parametric study of axle box acceleration at squats," *Proc. Inst. Mech. Eng. F, J. Rail Rapid Transit*, vol. 229, no. 8, pp. 841–851, 2015.

[11] S. Kaewunruen, "Monitoring structural deterioration of railway turnout systems via dynamic wheel/rail interaction," *Case Stud. Nondestruct. Test. Eval.*, vol. 1, pp. 19–24, Apr. 2014.

[12] P. Salvador, V. Naranjo, R. Insa, and P. Teixeira, "Axlebox accelerations: Their acquisition and time–frequency characterisation for railway track monitoring purposes," *Measurement*, vol. 82, pp. 301–312, Mar. 2016.

[13] E. Kassa and J. C. O. Nielsen, "Dynamic interaction between train and railway turnout: Full-scale field test and validation of simulation modelss," *Vehicle Syst. Dyn.*, vol. 46, pp. 521–534, Sep. 2008.

[14] C. Esveld, *Modern Railway Track*. Zaltbommel, The Netherlands: MRT-Productions, 2001, pp. 122–123.

[15] D. Gabor, "Theory of communication. Part 1: The analysis of information," *J. Inst. Elect. Eng.*, vol. 93, no. 26, pp. 429–441, Jul. 1946.

[16] M. Vetterli and J. Kovacevic, *Wavelets and Subband Coding*. Englewood Cliffs, NJ, USA: Prentice-Hall, 2007.

[17] J. de Ville, "Théorie et applications de la notion de signal analytique," *Cables Transmiss.*, vol. 2, no. 1, pp. 61–74, 1948.

[18] Q. Wu, Y. D. Zhang, and M. G. Amin, "Continuous structure based Bayesian compressive sensing for sparse reconstruction of time-frequency distributions," in *Proc. 19th Int. Conf. Digit. Signal Process.*, Hong Kong, Aug. 2014, pp. 831–836.

[19] M. G. Amin, B. Jokanovic, Y. D. Zhang, and F. Ahmad, "A sparsity-perspective to quadratic time–frequency distributions," *Digit. Signal Process.*, vol. 46, pp. 175–190, Nov. 2015.

[20] E. Sejdić, I. Orović, and S. Stanković, "Compressive sensing meets time–frequency: An overview of recent advances in time–frequency processing of sparse signals," *Digit. Signal Process.*, to be published, doi: 10.1016/j.dsp.2017.07.016.

[21] S. Liu, Y. D. Zhang, T. Shan, and R. Tao, "Structure-aware Bayesian compressive sensing for frequency-hopping spectrum estimation with missing observations," *IEEE Trans. Signal Process.*, vol. 66, no. 8, pp. 2153–2166, Apr. 2018.

[22] I. Daubechies, J. Lu, and H. T. Wu, "Synchrosqueezed wavelet transforms: An empirical mode decomposition-like tool," *Appl. Comput. Harmon. Anal.*, vol. 30, no. 2, pp. 243–261, Mar. 2011.

[23] N. E. Huang *et al.*, "The empirical mode decomposition and the Hilbert spectrum for nonlinear and non-stationary time series analysis," *Proc. Roy. Soc. London A, Math., Phys. Eng. Sci.*, vol. 454, no. 1971, pp. 903–995, Mar. 1998.

[24] A. Garinei, G. Risitano, L. Scappaticci, and F. Castellani, "An optimized method to evaluate the performance of trench isolation for railway-induced vibration," *Measurement*, vol. 94, pp. 92–102, Dec. 2016.

[25] Z. Li, M. Molodova, A. Núñez, and R. Dollevoet, "Improvements in axle box acceleration measurements for the detection of light squats in railway infrastructure," *IEEE Trans. Ind. Electron.*, vol. 62, no. 7, pp. 4385–4397, Jul. 2015.

[26] L. Stanković, D. Mandić, M. Daković, and M. Brajović, "Time-frequency decomposition of multivariate multicomponent signals," *Signal Process.*, vol. 142, pp. 468–479, Jan. 2018.
[27] J. P. Amezquita-Sanchez and H. Adeli, "A new music-empirical wavelet transform methodology for time–frequency analysis of noisy nonlinear and non-stationary signals," *Digit. Signal Process.*, vol. 45, pp. 55–68, Oct. 2015.
[28] T. Oberlin, S. Meignen, and V. Perrier, "Second-order synchrosqueezing transform or invertible reassignment? Towards ideal time-frequency representations," *IEEE Trans. Signal Process.*, vol. 63, no. 5, pp. 1335–1344, Mar. 2015.
[29] B. Boashash, N. A. Khan, and T. Ben-Jabeur, "Time–frequency features for pattern recognition using high-resolution TFDs: A tutorial review," *Digit. Signal Process.*, vol. 40, pp. 1–30, May 2015.
[30] D. Bhati, M. Sharma, R. B. Pachori, and V. M. Gadre, "Time–frequency localized three-band biorthogonal wavelet filter bank using semidefinite relaxation and nonlinear least squares with epileptic seizure EEG signal classification," *Digit. Signal Process.*, vol. 62, pp. 259–273, Mar. 2017.
[31] S. Wang, X. Chen, G. Cai, B. Chen, X. Li, and Z. He, "Matching demodulation transform and synchrosqueezing in time–frequency analysis," *IEEE Trans. Signal Process.*, vol. 62, no. 1, pp. 69–84, Jan. 2014.
[32] N. A. Khan and M. Sandsten, "Time–frequency image enhancement based on interference suppression in Wigner–Ville distribution," *Signal Process.*, vol. 127, pp. 80–85, Oct. 2016.
[33] J. Pons-Llinares, J. A. Antonino-Daviu, M. Riera-Guasp, S. B. Lee, T.-J. Kang, and C. Yang, "Advanced induction motor rotor fault diagnosis via continuous and discrete time–frequency tools," *IEEE Trans. Ind. Electron.*, vol. 62, no. 3, pp. 1791–1802, Mar. 2015.
[34] A. T. Tzallas, M. G. Tsipouras, and D. I. Fotiadis, "Epileptic seizure detection in EEGs using time–frequency analysis," *IEEE Trans. Inf. Technol. Biomed.*, vol. 13, no. 5, pp. 703–710, Sep. 2009.
[35] H. Wang *et al.*, "Detection of contact wire irregularities using a quadratic time–frequency representation of the pantograph–catenary contact force," *IEEE Trans. Instrum. Meas.*, vol. 65, no. 6, pp. 1385–1397, Jun. 2016.
[36] M. Tarabini, S. Solbiati, B. Saggin, and D. Scaccabarozzi, "Setup for the measurement of apparent mass matrix of standing subjects," *IEEE Trans. Instrum. Meas.*, vol. 65, no. 8, pp. 1856–1864, Aug. 2016.
[37] M. Oregui, Z. Li, and R. Dollevoet, "An investigation into the modeling of railway fastening," *Int. J. Mech. Sci.*, vol. 92, pp. 1–11, Mar. 2015.
[38] K. Knothe and Y. Wu, "Receptance behaviour of railway track and subgrade," *Arch. Appl. Mech.*, vol. 68, nos. 7–8, pp. 457–470, 1998.
[39] S. Kaewunruen and A. M. Remennikov, "Progressive failure of prestressed concrete sleepers under multiple high-intensity impact loads," *Eng. Struct.*, vol. 31, no. 10, pp. 2460–2473, Oct. 2009.
[40] J. Smutny, "Measurement and analysis of dynamic and acoustic parameters of rail fastening," *NDT E Int.*, vol. 37, no. 2, pp. 119–129, 2004.
[41] A. P. de Man, "Dynatrack: A survey of dynamic railway track properties and their quality," Ph.D. dissertation, Dept. Structural Eng., Delft Univ. Technol., Delft, The Netherlands, 2002.
[42] N. Vincent and D. J. Thompson, "Track dynamic behaviour at high frequencies. Part 2: Experimental results and comparisons with theory," *Vehicle Syst. Dyn.*, vol. 24, pp. 100–114, Jan. 1995.
[43] M. Oregui, Z. Li, and R. Dollevoet, "Identification of characteristic frequencies of damaged railway tracks using field hammer test measurements," *Mech. Syst. Signal Process.*, vols. 54–55, pp. 224–242, Mar. 2015.
[44] M. Batel, "Operational modal analysis-another way of doing modal testing," *Sound Vibrat.*, vol. 36, no. 8, pp. 22–27, 2002.
[45] S. Gade, N. Møller, H. Herlufsen, and H. Konstantin-Hansen, "Frequency domain techniques for operational modal analysis," in *Proc. 1st Int. Oper. Modal Anal. Conf.*, 2005, pp. 1–10.
[46] A. Remennikov and S. Kaewunruen, "Experimental investigation on dynamic railway sleeper/ballast interaction," *Experim. Mech.*, vol. 46, no. 1, pp. 57–66, 2006.
[47] N. M. M. Maia and J. M. M. Silva, *Theoretical and Experimental Modal Analysis*. Taunton, U.K.: Research Studies Press, 1997, pp. 102–103.
[48] D. L. Brown, R. J. Allemang, and A. W. Phillips, "Forty years of use and abuse of impact testing: A practical guide to making good FRF measurements," in *Proc. 33rd Int. Modal Anal. Conf. (IMAC)*, vol. 8. Orlando, FL, USA, 2015, pp. 221–241.
[49] H. Feng, Z. Jiang, F. Xie, P. Yang, J. Shi, and L. Chen, "Automatic fastener classification and defect detection in vision-based railway inspection systems," *IEEE Trans. Instrum. Meas.*, vol. 63, no. 4, pp. 877–888, Apr. 2014.
[50] M. Guerrieri, G. Parla, and C. Celauro, "Digital image analysis technique for measuring railway track defects and ballast gradation," *Measurement*, vol. 113, pp. 137–147, Jan. 2018.
[51] Z. Wei, C. Shen, Z. Li, and R. Dollevoet, "Wheel–rail impact at crossings: Relating dynamic frictional contact to degradation," *J. Comput. Nonlinear Dyn.*, vol. 12, no. 4, p. 041016, 2017.
[52] B. J. Schwarz and M. H. Richardson, "Introduction to operating deflection shapes," *CSI Rel. Week*, vol. 10, pp. 121–126, Oct. 1999.
[53] Y. Li, H. Trinh, N. Haas, C. Otto, and S. Pankanti, "Rail component detection, optimization, and assessment for automatic rail track inspection," *IEEE Trans. Intell. Transp. Syst.*, vol. 15, no. 2, pp. 760–770, Apr. 2014.
[54] A. Jamshidi *et al.*, "A big data analysis approach for rail failure risk assessment," *Risk Anal.*, vol. 37, no. 8, pp. 1495–1507, 2017.
[55] G. Krummenacher, C. S. Ong, S. Koller, S. Kobayashi, and J. M. Buhmann, "Wheel defect detection with machine learning," *IEEE Trans. Intell. Transp. Syst.*, to be published, doi: 10.1109/TITS.2017.2720721.
[56] X. Gibert, V. M. Patel, and R. Chellappa, "Deep multitask learning for railway track inspection," *IEEE Trans. Intell. Transp. Syst.*, vol. 18, no. 1, pp. 153–164, Jan. 2017.
[57] *Evaluation of Measurement Data—Guide to the Expression of Uncertainty in Measurement*, document JCGM 100, BIPM, IEC, IFCC, ILAC, IUPAC, IUPAP, ISO, and OIML, 2008.

Zilong Wei received the M.S. degree in highway and railway engineering from Tongji University, Shanghai, China, in 2012. He is currently pursuing the Ph.D. degree in railway engineering with the Department of Engineering Structures, Delft University of Technology, Delft, The Netherlands.

His current research interests include track dynamics, condition monitoring of track infrastructure, frictional wheel–rail contact behavior, and crossing degradation.

Anthonie Boogaard received the M.S. degree in mechanical engineering (with a specialization in engineering dynamics) from the Delft University of Technology, Delft, The Netherlands, in 2012, where he is currently pursuing the Ph.D. degree in railway engineering with the Department of Engineering Structures.

He is involved in a research program, especially on the dynamics of switches and crossings. The aim is to better understand its behavior and to derive its condition from the vibration measurements.

Alfredo Núñez (M'02–SM'14) received the Ph.D. degree in electrical engineering from the Universidad de Chile, Santiago, Chile, in 2010.

He was a Post-Doctoral Researcher with the Delft Center for Systems and Control, Delft, The Netherlands. He is currently with the Section of Railway Engineering, Delft University of Technology, Delft. He is currently a Work Package Leader in the development of new sensor technologies (static, moving, and crowd-based sensors) for railway networks in Romania, Turkey, and Slovenia, in the European project H2020 NeTIRail-INFRA. He has authored a book titled *Hybrid Predictive Control for Dynamic Transport Problems* in the Series of *Advances in Industrial Control* (Springer-Verlag, 2013). He has co-authored hundreds of international journal papers and international conference papers. His current research interests include the maintenance of railway infrastructures, intelligent conditioning monitoring in railway systems, big data, risk analysis, and optimization.

Zili Li received the B.Sc. and M.Sc. degrees in mechanical engineering from Southwest Jiaotong University, Chengdu, China, in 1988 and 1991, respectively, and the Ph.D. degree in computational mechanics on numerical solution of rolling contact from the Delft University of Technology, Delft, The Netherlands, in 2002.

From 1999 and 2005, he was with the Institute of Road Transportation, TNO, Delft, where he was involved in research and software development of multibody dynamics and finite element method for crash safety. In 2005, he joined the Faculty of Civil Engineering and GeoSciences, Delft University of Technology, where he taught and performed research on railway engineering. He is currently a Full-Time Professor with the Section of Railway Engineering, Delft University of Technology. His current research interests include health monitoring and asset management of railway infrastructure, numerical solution of frictional rolling contact and its applications to analyses of wear, rolling contact fatigue, and vehicle dynamics, train–track interaction, particularly in the high-frequency/short-wave range and at switches and crossings, and friction adhesion between wheel and rail.

Dr. Li is the Chair of the Group of Rail Systems and Monitoring.

Rolf Dollevoet received the M.Sc. degree in mechanical engineering from the Eindhoven University of Technology, Eindhoven, The Netherlands, in 2003, and the Ph.D. degree in rail research on rolling contact fatigue from the University of Twente, Enschede, The Netherlands, in 2010.

Since 2003, he has been with the Railway Sector, ProRail, Utrecht, The Netherlands. Since 2012, he has been appointed as a Part-Time Professor with the Section of Railway Engineering, Delft University of Technology, Delft, The Netherlands. He was also a Railway System Expert with ProRail, where he was responsible for all the scientific research and innovation with the Civil Engineering Division, ProRail Asset Management.

Dr. Dollevoet was a recipient of the Jan van Stappen Spoorprijs 2010 Award (a yearly prize for contributions to the travel quality and service for passengers in The Netherlands) from the railway sector for his Ph.D. research and its huge potential to reduce track maintenance costs.